A Comparison of Stratospheric Gravity Waves in a High-Resolution General Circulation Model with 3-D Satellite Observations

H. Okui[1], C. J. Wright[2], N. P. Hindley[2], E. J. Lear[2], and K. Sato[1]

[1] Department of Earth and Planetary Science, The University of Tokyo, Tokyo, Japan.

[2] Centre for Space, Atmospheric and Oceanic Science, University of Bath, Bath, UK.

Corresponding author: Haruka Okui (okui@eps.s.u-tokyo.ac.jp)

Key Points:

- Stratospheric gravity waves (GWs) in a GW-permitting high-top general circulation model are validated globally for a boreal winter
- The global characteristics of GWs and their variation during a sudden stratospheric warming are explored using the 3-D Stockwell transform
- Better model representation of convection and higher vertical resolution of the nadir-viewing instrument could provide better GW coverage

Abstract

Atmospheric gravity waves (GWs) play a key role in determining the thermodynamical structure of the Earth's middle atmosphere. Despite the small spatial and temporal scales of these waves, a few high-top general circulation models (GCMs) that can resolve them explicitly have recently become available. This study compares global GW characteristics simulated in one such GCM, the Japanese Atmospheric GCM for Upper-Atmosphere Research (JAGUAR), with those derived from three-dimensional (3-D) temperatures observed by the Atmospheric Infrared Sounder (AIRS) aboard NASA's Aqua satellite. The target period is from 15 December 2018 to 8 January 2019, including the onset of a major sudden stratospheric warming (SSW). The 3-D Stockwell transform method is used for GW spectral analysis. The amplitudes and momentum fluxes of GWs in JAGUAR are generally in good quantitative agreement with those in the AIRS observations in both magnitude and distribution. As the SSW event progressed, the GW amplitudes and eastward momentum flux increased at low latitudes in the summer hemisphere in both the model and observation datasets. Case studies demonstrate that the model is able to reproduce comparable wave events to those in the AIRS observations with some differences, especially noticeable at low latitudes in the summer hemisphere. Through a comparison between the model results with and without the AIRS observational filter applied, it is suggested that the amplitudes of GWs near the entrance or exit of an eastward jet streak are underestimated in AIRS observations.

Plain Language Summary

Atmospheric gravity waves play key roles in the dynamics of the stratosphere, mesosphere and thermosphere. Three-dimensional satellite observations and high-resolution general circulation models are of broad use to further our understanding of their global characteristics. This is the first study to make a quantitative comparison of the global distribution of the amplitudes and momentum fluxes of gravity waves in the gravity-wave-permitting high-top general circulation model (GCM), Japanese Atmospheric GCM for Upper-Atmosphere Research (JAGUAR), with those derived from three-dimensional temperature measurements by Atmospheric Infrared Sounder (AIRS) on NASA's Aqua satellite. Good agreement in both magnitude and distribution of gravity wave activity is demonstrated between the JAGUAR and AIRS temperatures. There are relatively large differences in tropical regions in the summer hemisphere, where convective gravity waves are expected to be dominant. Comparison of model-simulated gravity waves with and without the AIRS vertical resolution applied indicates that gravity waves near the entrance or exit of an eastward jet streak may be overlooked in AIRS observations.

1 Introduction

Atmospheric gravity waves (GWs) are of crucial importance for the dynamics of the Earth's middle atmosphere. Transporting energy and momentum, these waves play an essential role in driving the temperatures and circulations in the middle atmosphere away from the radiative equilibrium state. A major portion of the GW momentum flux is carried by waves generated in the lower atmosphere. Their sources include topography, jets and fronts, convection, and strong wind shear. They propagate upward and deposit momentum into the atmospheric layer where they break or dissipate. This momentum deposition, or GW forcing, is the main driver of the mesospheric circulation (e.g., Andrews et al., 1987). It also drives or modulates phenomena in the stratosphere, such as the quasi-biennial oscillation (e.g., Baldwin et al., 2001; Dunkerton, 1997; Sato & Dunkerton, 1997).

In recent years, there has been growing interest in the contribution of GWs to the onset of stratospheric sudden warmings (SSWs) and the whole atmospheric response to SSWs. Although SSWs themselves are caused by strong planetary wave forcing, several studies showed that not only planetary waves but also GWs contribute to the occurrence of vortex preconditioning for SSWs (e.g., Albers & Birner, 2014; Wright et al., 2010). SSWs also have a notable impact on the mesosphere. An elevated stratopause is a jump of the stratopause to an upper mesospheric height several days after an SSW (Manney et al., 2008, 2009). It has been shown that both planetary waves and GWs are responsible for the formation and/or descent of elevated stratopause events (e.g., Chandran et al., 2011, 2013; Limpasuvan et al., 2012, 2016; Okui et al., 2021; Siskind et al., 2010; Thurairajah et al., 2014; Tomikawa et al., 2012). In addition to the phenomena in the winter hemisphere as mentioned above, the roles of GWs in the modification of the global middle atmosphere associated with SSWs has received considerable attention: Interhemispheric coupling is a lag correlation between the dynamical activity in the winter polar stratosphere, as typified by SSWs, and the temperatures in the polar upper mesosphere in the summer hemisphere. Though the mechanism is not yet fully understood, it is widely accepted that GWs are one of the key factors in this phenomenon (Körnich & Becker, 2010; Smith et al., 2020; Yasui et al., 2021). As such, careful quantitative evaluation of GW activity before and after SSWs will help enhance our understanding of the dynamical mechanisms of these phenomena.

To understand global characteristics of GWs, high-resolution satellite observations are a key tool. Ern et al. (2018) produced a global climatology of GW parameters using two satellite infrared limb sounders: High Resolution Dynamics Limb Sounder (HIRDLS) and Sounding of the Atmosphere using Broadband Emission Radiometry (SABER). These limb sounders have quite high vertical resolutions, namely 1 km for HIRDLS and 2 km for SABER (e.g., Barnett et al., 2008; Gille et al., 2003, 2008; Wright et al., 2011). However, their horizontal resolutions are much poorer (several hundreds of kilometers) and only horizontal wavelengths along the line of sight of the instruments can be obtained. Thus, the horizontal wavelengths and, hence, momentum fluxes of GWs are very likely to be overestimated.

To fully comprehend GW structure, three-dimensional (3-D) observations and 3-D analysis methods are necessary. In contrast to limb sounding, nadir-viewing satellite instruments, such as the Atmospheric Infrared Sounder (AIRS) on NASA's Aqua satellite, are characterized by high horizontal resolutions and low vertical resolutions. One approach to consistently observe 3-D GW structure is combining limb- and nadir-sounding instruments (Alexander & Teitelbaum, 2011; Wright et al., 2016a, 2016b). In addition, the recent development of 3-D spectral analysis techniques (Ern et al., 2017; Hindley et al., 2019; Wright et al., 2017, 2021) has made global 3-D GW measurements possible using the 3-D temperature retrieval for AIRS (Hoffmann & Alexander 2009).

Evaluation of the impact of observational filters on GW characteristics is also needed. Observational filters are limitations in observable spectral range depending on instruments and observational techniques. These filters for satellite instruments are determined by the sensitivity and sampling geometry. In this sense, intercomparison of satellite observations is worthwhile. Wright et al. (2011) compared the Constellation Observing System for Meteorology Ionosphere and Climate (COSMIC), HIRDLS and SABER. Similarly, Meyer et al. (2018) made a global comparison between AIRS and HIRDLS. These two studies showed that these instruments basically give close agreement in the relative distribution of large amplitudes but those having coarser vertical resolutions fail to obtain significant parts of a GW spectrum.

Recently, GW-permitting high-top GCMs have become available. As an example of this, Watanabe et al. (2022) visualized 3-D structure and propagation of GWs in a T639L340 whole neutral atmosphere GCM called the Japanese Atmospheric GCM for Upper Atmosphere Research (JAGUAR, Watanabe & Miyahara, 2009). JAGUAR is capable of reproducing the universal spectrum (e.g., VanZandt, 1985; Tsuda et al., 1989; Sato et al., 2003) , which is characterized by a steep slope of vertical wavenumber (m) spectra ($\propto \sim m^{-3}$) at high wavenumbers of m= ~10^{-4}–10^{-3} m^{-1} (Okui et al., 2022). Kruse et al. (2022), meanwhile demonstrated extremely good skill for four state-of-the-art numerical weather prediction models at reproducing AIRS-observed orographic waves around the Drake Passage. While two of the four models in this study were local-area in nature, two others, namely the Integrated Forecast System (IFS) and the Icosahedral Nonhydrostatic (ICON) model, were run globally with vertical domains from the surface up to ~80 km. Finally, Vadas and Becker (2018) and Becker and Vadas (2018) demonstrated secondary generation of GWs caused by primary orographic GWs using the Kühlungsborn Mechanistic general Circulation Model (KMCM; Becker, 2009). Becker and Vadas (2020) later extended the height range of this model to ~450 km, renaming it to the High Altitude Mechanistic general Circulation Model (HIAMCM). Using this model, Becker et al. (2022) nudged the troposphere, stratosphere and lower mesosphere of HIAMCM to reanalysis. They demonstrated that the model simulated a GW event over Northern Europe in January 2016 consistently with AIRS temperature measurements. However, although such GCMs can resolve a major part of GWs in the middle atmosphere, due to resolution limitations even in the perfect case it is still impossible for them to cover the whole spectral range of GWs.

Since no observations or model simulations can provide full information on the global characteristics of GWs, GW distributions and behavior should be carefully examined by intercomparing different models and instruments. Accordingly, Geller et al. (2013) compared absolute GW momentum fluxes in a 85-km-top high-resolution model, the Kanto model (Watanabe et al., 2008), with those derived from SABER and HIRDLS observations. The Kanto model, the predecessor of the JAGUAR model, and a low-top high-resolution model, Community Atmosphere Model, version 5 (CAM5) in general agreed better with the observations than other climate models did. Regarding the state-of-the-art GW-permitting high-top GCMs mentioned above, validation of model-simulated GWs using observations is mostly limited to local comparisons (Becker et al., 2022; Kruse et al., 2022). The global distribution of GW momentum flux, combined with careful GW validation and examination of the spectral coverage, will also be informative for improvement of GW parameterization schemes.

In this study, we compare global GW characteristics between hindcast simulations performed with JAGUAR and 3-D AIRS observations. In doing so, we validate the GWs in JAGUAR against AIRS and, in addition, are able to estimate the possible impact of the coarse vertical resolution of AIRS on observed GWs by comparing two datasets from JAGUAR with and without a vertical low-pass filter acting as an analogue of AIRS' resolution limitations. In this paper, we show results from December 2018 to January 2019. This period contains an SSW whose onset occurred on 1 January 2019. Thus, variability in GW activity during the SSW event is also described.

This paper begins by describing details of the observations and model simulation and explaining the 3-D Stockwell (S-) transform, which we used for GW spectral analysis. Section 3 first addresses comparisons of global distribution of GW amplitude and momentum flux and their variability before and after the 2019 SSW. Then, we take a closer look at some GW events.

Section 4 discusses the mechanisms of the distribution of GW characteristics described in the previous section, the effect of an SSW on GW activity, and possible reasons for the agreement and disagreement found in the AIRS and JAGUAR results. We summarize and provide some concluding remarks in Section 5.

2 Data and Methods

2.1 AIRS

AIRS is a nadir-sounding satellite instrument on NASA's Aqua satellite (Aumann et al., 2003; Chahine et al., 2006). The satellite flies in a sun-synchronous near-polar orbit, completing 14.55 orbits per day. Viewing in the nadir of the satellite, AIRS has a good ability to observe fine horizontal-scale structures. The instrument scans a continuous 1780 km-wide swath of 90 pixels with a horizontal resolution varying from ~13.5 km × 13.5 km at nadir to ~41 km × 21.4 km at track edge. The data are sectioned into 135-pixel along-track pieces, referred to as granules, whose lengths are roughly 2250 km. There are 240 granules per day, corresponding to 6 minutes of data collection each. AIRS has 2378 spectral channels. We analyze 3-D temperatures derived from AIRS infrared radiance measurements in the 4.3 and 15 μm infrared CO2 channels, retrieved using the method described by Hoffmann and Alexander (2009). The vertical resolution of the retrieved temperature is 7–20 km over an altitude range of z= 15–60 km (Hindley et al., 2019). The assumption of local thermodynamic equilibrium, used in the retrieval scheme, is violated during daytime and, to reduce this influence, the daytime retrieval only uses the 15 μm channel. As a result, the vertical resolution is coarser for the daytime retrieval (see Fig. 2b of Hindley et al., 2019). To examine a sufficient number of granules even at summer latitudes, we analyzed the global characteristics using both daytime and nighttime observations. In case studies presented in Section 3.3, only the results from nighttime observations are shown.

2.2 JAGUAR

Temperature perturbations in hindcast simulations performed with a GW-permitting GCM, JAGUAR, are compared with those in AIRS observations. JAGUAR is a hydrostatic global spectral model using a T639 triangular truncation, which is capable of resolving horizontal wavelengths longer than ~60 km (Watanabe & Miyahara, 2009). The model contains 340 vertical layers from the surface to the lower thermosphere (~150 km) with a constant log-pressure height interval of 300 m. No parameterization schemes for sub-grid-scale GWs are applied in this model. Cumulus convection is parameterized by using the scheme presented by Arakawa and Schubert (1974).

Hindcast simulations using JAGUAR were performed for boreal winter 2018–2019. The model was initialized by 3-day spectral nudging to a reanalysis dataset created by the JAGUAR-Data Assimilation System (JAGUAR-DAS; Koshin et al., 2020, 2022). This nudging process relaxes only the low total horizontal wavenumber (n) components of n= 0–15 to the reanalysis data, leaving GWs and other high n components ($n \geq 16$) free to evolve. Supporting this, the ERA5 reanalysis dataset (Hersbach et al., 2020) was used to constrain n= 0–15 in the troposphere (> 200 hPa), where the reliability of the JAGUAR-DAS reanalysis is relatively low compared to ERA5. After the initializations, a series of 4-day free-run simulations were performed. These free-runs from December 2018 to 8 January 2019 with a 4-day interval are analyzed in this study. The period contains an Arctic major SSW occurring around New Year's

Day in 2019 (Rao et al., 2019). The background wind field during this period, which can affect the generation, propagation and attenuation of GWs, significantly changed as a result of this event, and thus the averages shown in this study are taken individually over the separate periods of 15–22, 23–31 December 2018 and 1–8 January 2019, which correspond to a period with the stable stratospheric winter jet, and the periods before and after an SSW, respectively.

To provide a fair comparison with AIRS temperature perturbations, the temperature output from JAGUAR simulations was resampled as the AIRS footprints by using linear interpolation. Hindley et al. (2021), who compared GWs in a local-area configuration of the UK Met Office Unified Model (1.5 km grid, 118 vertical levels) with AIRS, first convolved the model-simulated temperature field with a horizontal Gaussian function with a full width at half maximum (FWHM) of 13.5 km×13.5 km and then resampled the model data as the AIRS footprints. In this study, such horizontal filters were not applied because there is no considerable difference in horizontal resolutions between JAGUAR and AIRS. Since the JAGUAR outputs were averaged to a 1-hour frequency, this resampling was performed on the JAGUAR data whose representative time (the central time of the averaged time period) is closest to the observation time of each AIRS granule. For example, Granule 127 on 16 December 2018, which corresponds to the AIRS observation from 13:42UTC to 13:48UTC on 16 December 2018, was compared with JAGUAR data at 13:30UTC on the same day.

The vertical resolution of the 3-D AIRS temperature retrieval was also applied to the JAGUAR temperatures. Before doing that, we extracted one model layer every three (i.e., at a constant log-pressure height interval of 900 m) to reduce computational cost. Since the vertical resolution of AIRS is coarser by an order of magnitude than 900 m, it is expected that the influence of this extraction on the results is limited. Then, the extracted model layers were linearly interpolated onto a regular geopotential height grid from the surface to z= 90 km in 1 km steps. We then used the method of the AIRS vertical resolution application described in Hindley et al. (2021). This involved calculating the convolution of the model temperature profiles using vertical Gaussian functions with FWHMs corresponding to the AIRS vertical resolution (see Fig. 2b of Hindley et al., 2019) for each altitude. Finally, we added noise to the model data to simulate the AIRS retrieval noise following the method described by Hindley et al. (2019). The residual perturbations (refer to Section 2.3 for the definition) in Granule 1 at 00:00 UTC on 15 December 2018, which contains no discernible waves, are horizontally randomized and added to the resampled JAGUAR granules.

To discuss the effect of the observational filter and retrieval noise, the results for JAGUAR without the applications of the AIRS vertical resolution and retrieval noise are also shown in Section 3. The model layers were interpolated onto a 300-m geopotential height grid for the preparation of these data. They are hereafter referred to as JAGUAR without the observational filter. On the other hand, JAGUAR with the observational filter denotes the model data with all the process described above applied. In addition to wave features, horizontal winds in JAGUAR are described in the following sections. Note that the altitudes on all the figures from JAGUAR are not the log-pressure height but the geopotential height.

2.3 The 3-D S-Transform

The N-dimensional S-transform (Stockwell et al., 1996) application developed by Hindley et al. (2019) was used here for spectral analysis of 3-D temperature perturbations. First, the method of GW extraction is as follows: AIRS temperatures and JAGUAR temperatures

resampled as AIRS footprints are interpolated onto a regular horizontal grid with a constant interval of 20 km. Fitting fourth-order polynomials in the cross-track direction, the background temperatures ($\bar{T}$) are extracted from the original temperature fields, following the method described in Alexander and Barnet (2007). The residual perturbations T', containing GWs and noise, are used for the spectral analysis. The resulting temperature perturbations are sensitive to waves having vertical wavelengths of $8 \lesssim \lambda_z \lesssim 40$ km and horizontal wavelengths λ_{H} from several tens of kilometres, depending on the angle from nadir, to $\lambda_{\mathrm{H}} \sim 1000$ km (Ern et al., 2017; Hindley et al., 2019; Hoffmann et al., 2014).

Second, the 3-D S-transform was performed. To exclude pixel-to-pixel variations, waves with shorter λ_z than a threshold vertical wavelength λ_{c} or shorter λ_{H} than 60 km were ignored. The threshold was set as $\lambda_{\mathrm{c}} = 6$ km for AIRS, 2 km for JAGUAR with the observational filter, and 1 km for JAGUAR without the observational filter. Only the dominant 1000 sets of wavenumbers in each granule are analyzed. The resulting 3-D S-transform object for each granule contains six-dimensional wave properties. To reduce the number of dimensions and computational expense, we only use the 3-D spatial structure of the properties of the dominant waves for each granule.

Rotating along- and cross-track wavenumbers by using the azimuth of the along-track direction at each grid, wave amplitude $|T'|$ and zonal, meridional and vertical wavenumbers (k, l, m) are finally obtained.Under the midfrequency assumption, namely $f \ll \hat{\omega} \ll N$ (f is the Coriolis parameter; $\hat{\omega}$ is the intrinsic frequency; and N is the buoyancy frequency), the zonal and meridional components of vertical GW momentum flux $\left(\mathrm{MF}_x, \mathrm{MF}_y\right)$ can be derived as

$$\left(\mathrm{MF}_x, \mathrm{MF}_y\right) = -\frac{\rho}{2}\left(\frac{\mathrm{g}}{N}\right)^2 \left(\frac{|T'|}{\bar{T}}\right)^2 \left(\frac{k}{m}, \frac{l}{m}\right) \quad (1)$$

where ρ is atmospheric density, and g is the acceleration due to gravity (Ern et al., 2004). To preserve the direction of $\left(\mathrm{MF}_x, \mathrm{MF}_y\right)$, the three components (k, l, m) of a wave vector are computed as signed values (Alexander et al., 2018).

3 Results

3.1 Global Features of GW Amplitudes and Momentum Fluxes

Global distributions of GW amplitudes and momentum fluxes are described in this section with a comparison between AIRS observations and JAGUAR hindcasts. Prior to that, we briefly give an overview of the evolution of the zonal wind field during the period of interest. We do this because the background wind field, which changed drastically due to the SSW, is expected to be highly correlated with GW characteristics. Figure 1 shows horizontal maps of the zonal wind at $z = 39$ km during 15–22 December 2018 (Period 1) in Fig. 1a, 23–31 December 2018 (Period 2) in Fig. 1b, and 1–8 January 2019 (Period 3) in Fig. 1c. All the horizontal maps in this paper are shown for $z = 39$ km, which lies in the center of the usable height range of AIRS data. The onset of the major warming occurred on 1 January 2019. During Period 1 (Fig. 1a), the eastward jet in the winter Northern Hemisphere is still strong. The polar vortex has shifted away from North America towards Europe. It has been shown previously that the Arctic polar vortex is inclined to be displaced towards the Eurasian Continent especially in recent years (e.g., Zhang et

al., 2016), and thus the zonal wind in Period 1 displays a pattern and strength that are similar to climatological boreal winters. In Period 2 from 23 December to just prior to the SSW onset (Fig. 1b), the polar vortex is located over the North Atlantic. The zonal wind in the Northern Hemisphere has zonally asymmetric structure with a zonal wavenumber s= 1. The summer westward jet at ~25° S is stronger than that in Period 1. After the onset of the major warming, or in Period 3 (Fig. 1c), westward wind has become dominant at high latitudes in the Northern Hemisphere. The summer jet has been continuously accelerated until this period.

Figure 2 displays the horizontal distribution of the amplitudes and momentum fluxes of stratospheric GWs in Period 1 from AIRS (Figs. 2a, 2c and 2e) and JAGUAR with the AIRS observational filter applied (Figs. 2b, 2d and 2f). The right-hand panel of each horizontal map shows the respective zonal-mean values. What stands out in this figure is the good agreement of the distribution and magnitude of peaks in the amplitudes between JAGUAR and AIRS data. High GW activities are distributed along the eastward jet in the Northern Hemisphere (Fig. 1a) and in the low-latitude region of the Southern Hemisphere. There are remarkably large amplitudes of ~3.5 K above the central and eastern Eurasia. This feature is quantitatively consistent between the model and the observations. Large amplitudes are also observed above Europe and the highest areas of the Ural mountains in Russia (~65° N, 60° E). The maxima of these features are 3–3.5 K in the AIRS observation and 2–2.5 K in the JAGUAR data. At low latitudes (~20° S) in the summer hemisphere, high-amplitude peaks can be seen in the eastern part of Southern America and near Madagascar Island. There is a background amplitude level of ~1.4 K in AIRS data which is almost uniform everywhere except in the areas of large amplitudes described above. This level shift is much smaller, specifically ~0.5 K, in the JAGUAR data, which may suggest that the method used of adding noise in the local-area study by Hindley et al (2019) is not well-suited for this purpose at global scales.

As shown in Figs. 2c and 2d, strong westward momentum flux is observed along the winter jet over the Eurasian Continent. Again, the peaks in this region from JAGUAR data show good quantitative agreement with the AIRS observations. In the low-latitude region in the Southern Hemisphere, there is eastward momentum flux both in the AIRS and JAGUAR data. The magnitude of this eastward momentum flux in eastern South America is slightly smaller in the JAGUAR data than in the AIRS observations. The zonal-mean MF_x at ~20° S is slightly larger in the results derived from the AIRS observations, with a value of ~0.3 mPa in the AIRS result and ~0.2 mPa in the JAGUAR result. The geographical pattern of meridional momentum flux is also mostly consistent between JAGUAR and AIRS. To the south (north) of the winter jet, meridional momentum flux is northward (southward) (Figs. 2e and 2f).

During 23–31 December 2018 (Period 2), as can be seen in Fig. 3, GW amplitudes and momentum fluxes in the Northern Hemisphere are much smaller than those during Period 1. On the other hand, eastward momentum flux at low latitudes in the Southern Hemisphere is slightly stronger than that in Period 1. These trends are continuously observed in Period 3 as well, as shown in Fig. 4.

3.2 The Observational Filter of AIRS

To estimate influence of the AIRS observational filter on the above AIRS results, comparisons of the amplitudes and momentum fluxes are made here between JAGUAR with and without the observational filter. Figure 5 displays the amplitudes, vertical wavelengths λ_z, and

momentum flux of stratospheric GWs in Period 1 estimated from the JAGUAR data without the vertical low-pass filter, which is an analogue of the observational filter of AIRS. Note that the color scales in Figs. 5a, 5c and 5d are different from those in panels (a, b), (c, d) and (e, f) in Figs. 2–4, respectively. GW amplitudes (Fig. 5a) in the raw model are approximately twice as large as those with the observational filter applied (Fig. 2b). The same relation applies to the GW momentum flux (Figs. 5c and 2d; 5d and 2f). The relative variations in the horizontal distribution of GW amplitudes and momentum flux without the observational filter are similar to those from AIRS and JAGUAR with the observational filter. Interestingly, however, amplitudes and momentum fluxes in eastern Eurasia are larger in the results from JAGUAR without the observational filter. In addition, relatively large amplitudes and poleward momentum fluxes are observed in the North Atlantic Ocean, which can hardly be seen in the results from AIRS or JAGUAR with the observational filter.

In other words, the most considerable underestimation due to the observational filter is observed in eastern Eurasia and the North Atlantic Ocean. These areas, denoted by the circles in Figs. 5a and 5b, correspond to relatively short λ_z (Fig. 5b) along the eastward jet in the Northern Hemisphere (shown by the dashed curve). Figure 6 shows the polar map of absolute horizontal wind speed at z= 39 km ($\sqrt{u^2 + v^2}$, where u and v are zonal and meridional wind) in Period 1. The areas being discussed here extend from the exit of one of the two jet streaks to the entrance of the other along the displaced and distorted polar vortex. The background winds in these areas are weak. Meyer et al. (2018) showed that GW variances observed by AIRS have higher correlation with background wind speed compared to variances observed by HIRDLS. They suggested that this is because the Doppler shift increases λ_z of GWs in regions with strong background winds, making them more easily observed by AIRS, which has lower vertical resolution. The larger impact of the AIRS observational filter near the exits and entrances of the jet streaks is consistent with their suggestion.

3.3 Case studies

To clarify the common features and differences of GWs in the AIRS observation and JAGUAR data, intercomparisons of T' in three granules are made in this section among AIRS and JAGUAR with and without the observational filter. Figure 7 displays T' at z= 39 km observed nighttime granules over Europe (hereafter Case 1), eastern Eurasia (Case 2), and to the east of Madagascar (Case 3). In Case 1, the AIRS data and JAGUAR with the observational filter contains similar wave structures (Figs. 7a and 7b). There are wave-like structure having short zonal wavelengths to the south of ~48° N, and phase fronts laying from south-southwest to north-northeast to the north of ~51° N in both of the data. The amplitudes of these waves are slightly stronger in the AIRS measurements than in JAGUAR with the observational filter. The latter wave, which can be seen in the north part of the AIRS granule, is dominant in a larger part of the result from JAGUAR without the observational filter (Fig. 7c).

In Case 2, strong, fine-scale waves whose phase fronts run meridionally are observed to the south of ~55° N both in the AIRS and JAGUAR with the observational filter, as shown in Figs. 7d and 7e. The overall structure of the temperature perturbations in the filtered JAGUAR data agrees well with that in the AIRS measurements. In addition to these waves, there are strong wave fronts bending at a latitude of ~58° N in JAGUAR without the observational filter applied

(Fig. 7f). The waves composing this V-shaped pattern are not clear in the AIRS measurements or in JAGUAR with the AIRS observational filter. This difference will be detailed below.

The most obvious differences between the AIRS and JAGUAR data are found at low latitudes in the Southern Hemisphere. The AIRS T' for Case 3 contains a plane wave whose phase fronts lay from northwest to southeast and a concentric wave whose center is located to the northwest of the granule (Fig. 7g). However, the plane wave does not have a noticeable amplitude and only the concentric wave can be seen in the JAGUAR data (Figs. 7h and 7i).

To investigate the reason why the V-shaped waves in Case 2 cannot be identified when the observational filter is applied, we examine the characteristics of the dominant waves in this V-shaped structure and the background thermodynamical field. Figure 8 provides the results from the 3-D S-transform of the temperature perturbations in JAGUAR without the observational filter. Amplitudes are large not only in the south part (< ~55° N) but also in the northeast part of the granule (Fig. 8a). The vertical wavelengths are λ_z= 5–13 km in the latter (northeast) region, which are shorter than the waves in the south region with $\lambda_z \gtrsim$ 20 km (Fig. 8b). The distribution of short λ_z in the full-resolution JAGUAR overlaps the region of small amplitudes in JAGUAR with the observational filter. This fact is consistent with the low vertical resolution and thus low sensitivity to waves having short λ_z of AIRS measurements.

GW meridional momentum flux to the north (south) of the bending point is southward (northward), as shown in Fig. 8d. It is noteworthy that eastward (i.e., positive) zonal momentum flux is observed in the south part of the V-shaped pattern in z= 32–41 km (Figs. 8c and 8g). This means eastward GWs propagating upward or westward GWs propagating downward are dominant there.

Figure 9 shows the zonal wind and N structure for Case 2. Strong eastward winds are found at latitudes of <58° N at z= ~30–65 km, while zonal wind is weak on the polar side of 60° N (Fig. 9a). In the upper stratosphere at z= 30–45 km inside the polar vortex, large N is observed as shown in Fig. 9b. Considering the dispersion relation for GWs having zonal wave vectors under the midfrequency assumption, $m^2 \approx N^2/(c-U)^2$ where c is ground-based phase velocity, short λ_z in small U and large N are a consistent consequence.

4 Discussions

Overall, JAGUAR has good skill in reproducing the characteristics of stratospheric GWs with large amplitudes observed by AIRS. On the other hand, the AIRS GW amplitude has a background level of 1.2–1.4 K, which is greater than that for the JAGUAR GW amplitude. These background amplitudes have almost no net contribution to the momentum flux. Hence, it is inferred that the background level seen in the AIRS amplitude is due to noise. The retrieval noise we added randomly to the JAGUAR data is not enough to simulate this, likely due to the uncorrelated nature of the noise source used (see e.g., figure 5.16 of Wright, 2010), and in future work we will investigate the use of more internally-correlated noise structures.

On the polar (equatorial) side of the winter jet, equatorward (poleward) momentum flux is predominant. This focusing effect of GW rays on the jet can be explained by wave refraction and advection. When waves propagate westward relative to the background winds, i.e., $\hat{c} = \hat{\omega}/k < 0$ and thus $k < 0$ in the formulation taking $\hat{\omega} > 0$, waves are refracted toward the eastward jet (e.g., Sato et al., 2009). This is because the time derivative of a meridional wavenumber

$d_g l/dt$ as measured by an observer moving with the local group velocity is induced by a meridional shear of the background zonal wind $\partial U/\partial y$ as:

$$\frac{d_g l}{dt} = -k\frac{\partial U}{\partial y} \tag{2}$$

according to ray-tracing theory (Jones, 1969). On the polar side of the eastward jet, negative $\partial U/\partial y$ decreases l for waves with $k < 0$. As a result, waves propagating upward and westward relative to U, whose m and k are both negative, tend to have negative MF_y. On the equatorial side, positive $\partial U/\partial y$ increases l, resulting in $\mathrm{MF}_y > 0$. In addition, once the wavevector of a GW becomes toward the jet axis, the component of the background wind projected in the direction orthogonal to the wavevector will point to the jet axis. As a result, waves are advected toward the jet axis (see Fig. 6 of Sato et al., 2012). Since most GW parameterization schemes ignore lateral propagation of GWs, this focusing of negative MF_x on the jet axis due to refraction and advection is considered to be one of the causes of the well-known "cold-pole problem". The good agreement of the JAGUAR's GW momentum fluxes along the jet with the AIRS observations supports the usefulness of this model for studies on this problem.

Interestingly, GW amplitudes and momentum fluxes in the low-latitude Southern Hemisphere increased during SSW development. A possible cause of this is the acceleration of the westward wind in this region (Fig. 1). The stronger the westward wind is, the larger the fraction of GWs propagating eastward relative to the background wind can propagate upward. Several studies have reported that a cooling in the equatorial stratosphere occurs simultaneously with an SSW (Fritz & Soules,1970; Julian & Labitzke, 1965). This cooling is induced by strong planetary wave forcing in the winter stratosphere (e.g., Randel, 1993). This results in acceleration of the westward wind above and on the polar side of the cooling region due to the poleward temperature gradient and the thermal wind relationship. Another possible cause is that more GWs were generated in the tropical troposphere when the SSW occurred. Several studies found that cooling in the tropical lower stratosphere (e.g., Kodera & Yamada, 2004; Kodera et al., 2011) and/or upwelling extending in the tropical stratosphere and troposphere itself (Yoshida & Mizuta, 2021) enhance tropical convection during SSWs. This enhanced convection may have generated more GWs propagating into the tropical stratosphere. However, we found that there was no significant long-lasting enhancement in the upwelling at 100 hPa in 5° S–25° S which persists for as long as the negative MF_x enhancement (not shown). Thus, the acceleration of the westward jet in the summer stratosphere is a more plausible cause.

With regard to GW reproducibility, the comparison with the AIRS observations demonstrates that the JAGUAR model simulates GW features along the winter jet skillfully. Relatively speaking, however, larger differences were observed between GWs in the southern low-latitude region in JAGUAR and those in AIRS. Since the model is a hydrostatic GCM and cumulus convection is parameterized, GW generation due to convection is not properly expressed and may be underestimated. The underestimation of convective GWs may be the reason of the lower GW activity in the summer low-latitude region.

Comparing the results from JAGUAR with and without the AIRS observational filter applied, we showed that the observational filter, or the low vertical resolution of AIRS, reduces GW amplitudes and momentum fluxes in the model approximately by half. Despite this, the impact on the relative horizontal distribution of GW characteristics was limited. This finding

consistent with that of Meyer et al. (2018) who compared GWs in AIRS measurements with those in HIRDLS measurements.

The most interesting aspect of our results on the impact of the observational filter is that more GWs were filtered out near the exits and entrances of the two jet streaks. The exit of a jet streak is the place where spontaneous-adjustment emission of GWs occurs (e.g., Dörnbrack et al., 2018; Plougonven and Zhang, 2014; Yasuda et al., 2015). In Case 2 in Section 3.3, the eastward MF_x observed near the jet (Figs. 8c and 8g) suggests downward propagation of westward GWs, considering the background wind is eastward. This fact indicates that these waves originate from the jet. The V-shaped phase fronts of these waves shown in Fig. 7f are similar to theoretically-derived phase structure of GWs emitted from spontaneous adjustment. Then, why did these waves have short λ_z, which are filtered out by the observational filter? In general, around the exit or entrance of a jet streak, horizontal wind is not as strong as in the jet core. The static stability N^2 is high in the middle and upper stratosphere inside the polar vortex due to the GW-driven winter polar stratopause. In addition, a Q-vector convergence exists on the polar side of the jet exit region, which induces upwelling. This upwelling may contribute to the formation of high N^2 above. These weak horizontal winds and high N^2 make λ_z of GWs shorter, making it difficult to resolve them with AIRS. Regarding the background winds and N^2, conditions in both the exit and entrance regions of jet streaks are almost the same. In the exit regions of jet streaks, the wave capture mechanism may also contribute to the small λ_z (Bühler & McIntyre, 2005). According to this mechanism, GWs heading for the jet exit come to have large negative (positive) vertical wavenumbers on the top (bottom) edge of the exit of a jet streak, regardless of their source structure.

5 Summary and Concluding Remarks

A comparison of stratospheric GWs in the GW-permitting GCM, JAGUAR with 3-D temperature measurements by AIRS has been made for the period of 15 December 2018–8 January 2019. The two datasets show surprisingly good quantitative agreement in:

1. The peaks in the amplitudes and zonal and meridional momentum fluxes of GWs
2. The distribution of GW characteristics: high GW activity in Europe, over the Ural Mountains, in eastern Eurasia, and in the low-latitude region in the summer hemisphere
3. The attenuation and reinforcement of GWs along the winter eastward jet and summer westward jet during the SSW occurrence, respectively

At the same time, some differences have also been observed:

4. The results indicate that GWs at low latitudes are underestimated by JAGUAR. A possible reason for this is that the model cannot sufficiently reproduce convective GWs.
5. The background level in the AIRS GW amplitudes cannot be fully explained by the retrieval noise added to JAGUAR GWs. There is almost no net momentum flux associated with the background amplitudes. We hypothesize that this is due to the internally-uncorrelated nature of the noise added.

Regarding (4), this may be due to low reproducibility of convection in the model. JAGUAR is a hydrostatic model, and a cumulous parameterization scheme is adopted in it. In general, cumulous parameterizations are not designed to reproduce GW generation associated with

493 convection, which can be a reason for the low GW activity at low latitudes in the model. Further
494 research using a non-hydrostatic and cloud-resolving model would be interesting to assess the
495 impact of the model configuration of JAGUAR on the GW reproducibility.

496 The influence of the AIRS observational filter has been also estimated by comparing the
497 model results with and without the filter applied. Approximately half of the GW amplitude in the
498 full-resolution JAGUAR was filtered out by the observational filter. At large scales, the relative
499 horizontal distribution was not dramatically changed. However, the regions of large GW
500 amplitude near the entrances or exits of the eastward jet streaks are affected strongly by the
501 observational filter. It has been reported that GWs are generated by spontaneous adjustment near
502 the exit of a jet streak (e.g., Dörnbrack et al., 2018). Conducting a case study, we found that the
503 distribution of V-shaped GWs near the jet exit, which were filtered out due to short λ_z, matched
504 with the regions of weak zonal wind and high N^2. These two conditions, weak winds and high
505 N^2, are likely to be met on the polar side of the polar vortex in the middle and upper stratosphere.
506 These results suggest that studies on spontaneous-adjustment emission of GWs using AIRS
507 observations need to pay attention to this aspect.

508 Notwithstanding the limitation that the results have been described only for one boreal
509 winter, the validation of the JAGUAR model we made here supports the effectiveness of this
510 model for various studies on GWs in the middle atmosphere. Performing multi-year hindcast
511 simulations with the model could produce the climatological dataset of the GW momentum flux
512 in the whole middle atmosphere. Such a dataset, validated by comparison with long-term
513 observations, would be a useful guideline for the source parameters in non-orographic GW
514 parameterizations.

515

516 **Acknowledgments**

517 This work was supported by JSPS KAKENHI Grant Numbers JP21J20798 supporting H. Okui
518 and JP22H00169 supporting H. Okui and K. Sato, by Royal Society University Research
519 Fellowship URF\R\221023 and Research Grant RGF\R1\180010 supporting C. J. Wright, and by
520 NERC grants NE/S00985X/1 and NE/W003201/1 supporting C. J. Wright and N. Hindley.
521

522 **Open Research**

523 The AIRS temperature data set is derived using AIRS radiances, which are freely available from
524 NASA's GES DISC at https://disc.gsfc.nasa.gov/ website, by the retrieval method described in
525 Hoffmann and Alexander (2009). The processed AIRS data and JAGUAR hindcast outputs are
526 available from https://pansy.eps.s.u-tokyo.ac.jp/archive_data/Okui_etal_AIRS_2023/. R2022b
527 version of the MATLAB used for spectral analysis of gravity waves and producing figures is
528 presented at https://jp.mathworks.com/products/matlab.html. Figures 1 and 6 were produced
529 using the GFD DENNOU Library (https://www.gfd-dennou.org/arch/dcl/dcl-7.5.1/).
530

531 **References**

Albers, J. R., & Birner, T. (2014). Vortex Preconditioning due to Planetary and Gravity Waves prior to Sudden Stratospheric Warmings. *Journal of the Atmospheric Sciences*, **71**(11), 4028–4054. https://doi.org/10.1175/JAS-D-14-0026.1

Alexander, M. J., & Barnet, C. (2007). Using Satellite Observations to Constrain Parameterizations of Gravity Wave Effects for Global Models, *Journal of the Atmospheric Sciences*, **64**(5), 1652–1665. https://doi.org/10.1175/JAS3897.1

Alexander P., Schmidt T., & de la Torre, A. (2018). A method to determine gravity wave net momentum flux, propagation direction, and "real" wavelengths: A GPS radio occultations soundings case study. *Earth and Space Science*, **5**, 222–230. https://doi.org/10.1002/2017EA000342

Alexander, M. J., & Teitelbaum, H. (2011). Three-dimensional properties of Andes mountain waves observed by satellite: A case study. *Journal of Geophysical Research*, **116**, D23110. https://doi.org/10.1029/2011JD016151

Arakawa, A., & Schubert, W. H. (1974). Interaction of a Cumulus Cloud Ensemble with the Large-Scale Environment, Part I. *Journal of Atmospheric Sciences*, **31**(3), 674-701. https://doi.org/10.1175/1520-0469(1974)031%3C0674:IOACCE%3E2.0.CO;2

Aumann, H., Chahine, M., Gautier, C., Goldberg, M., Kalnay, E., McMillin, L., et al. (2003). AIRS/AMSU/HSB on the aqua mission: design, science objectives, data products, and processing systems. *IEEE Transactions on Geoscience and Remote Sensing*, **41**, 253–264. https://doi.org/10.1109/tgrs.2002.808356

Baldwin, M., Gray, L., Dunkerton, T., Hamilton, K., Haynes, P., Randel, W., et al. (2001). The quasi-biennial oscillation. *Reviews of Geophysics*, **39**(2), 179–229. https://doi.org/10.1029/1999RG000073

Barnett, J. J., Hepplewhite, C. L., Osprey, S., Gille, J. C., & Khosravi, R. (2008). Cross-validation of HIRDLS and COSMIC radio occultation retrievals, particularly in relation to fine vertical structure. *Proceedings of SPIE*, **7082**, 708216. https://doi.org/10.1117/12.800702

Becker, E. (2009). Sensitivity of the Upper Mesosphere to the Lorenz Energy Cycle of the Troposphere. *Journal of the Atmospheric Sciences*, **66**(3), 647–666. https://doi.org/10.1175/2008JAS2735.1

Becker, E., & Vadas, S. L. (2018). Secondary gravity waves in the winter mesosphere: Results from a high-resolution global circulation model. *Journal of Geophysical Research: Atmospheres*, **123**, 2605–2627. https://doi.org/10.1002/2017JD027460

Becker, E., & Vadas, S. L. (2020). Explicit global simulation of gravity waves in the thermosphere. *Journal of Geophysical Research: Space Physics*, **125**, e2020JA028034. https://doi.org/10.1029/2020JA028034

Becker, E., Vadas, S. L., Bossert, K., Harvey, V. L., Zülicke, C., & Hoffmann, L. (2022). A high-resolution whole-atmosphere model with resolved gravity waves and specified large-scale dynamics in the troposphere and lower stratosphere. *Journal of Geophysical Research: Atmospheres*, **127**, e2021JD035018. https://doi.org/10.1029/2021JD035018

Bühler, O., & McIntyre, M. E. (2005). Wave capture and wave–vortex duality. *Journal of Fluid Mechanics*, **534**, 67–95. https://doi.org/10.1017/s0022112005004374

Chahine, M. T., Pagano, T. S., Aumann, H. H., Atlas, R., Barnet, C., Blaisdell, J., et al. (2006). AIRS, *Bulletin of the American Meteorological Society*, **87**, 911–926. https://doi.org/10.1175/bams-87-7-911

Chandran, A., Collins, R.L., Garcia, R.R., & Marsh, D. R. (2011). A case study of a spontaneously generated elevated stratopause generated in the Whole Atmosphere Community Climate Model. *Geophysical Research Letters*, **38**, L08804. https://doi.org/10.1029/2010GL046566

Chandran, A., Collins, R. L., Garcia, R. R., Marsh, D. R., Harvey, V. L., Yue, J., and de la Torre, L. (2013). A climatology of elevated stratopause events in the whole atmosphere community climate model. *Journal of Geophysical Research: Atmospheres*, **118**, 1234–1246. https://doi.org/10.1002/jgrd.50123

Dunkerton, T. J. (1997). The role of gravity waves in the quasi-biennial oscillation. *Journal of Geophysical Research*, **102**(D22), 26053–26076. https://doi.org/10.1029/96JD02999

Dörnbrack, A., Gisinger, S., Kaifler, N., Portele, T. C., Bramberger, M., Rapp, M., et al. (2018). Gravity waves excited during a minor sudden stratospheric warming, *Atmospheric Chemistry and Physics*, **18**, 12915–12931, https://doi.org/10.5194/acp-18-12915-2018

Fritz, S., & Soules, S. D. (1970). Large-scale temperature changes in the stratosphere observed from Nimbus III. *Journal of the Atmospheric Sciences*, **27**, 1091−1097. https://doi.org/10.1175/1520-0469(1970)027%3C1091:LSTCIT%3E2.0.CO;2

Ern, M., Hoffmann, L., & Preusse, P. (2017). Directional gravity wave momentum fluxes in the stratosphere derived from high-resolution AIRS temperature data. *Geophysical Research Letters*, **44**, 475–485. https://doi.org/10.1002/2016GL072007

Ern, M., Trinh, Q. T., Preusse, P., Gille, J. C., Mlynczak, M. G., Russell Iii, J. M., & Riese, M. (2018). GRACILE: a comprehensive climatology of atmospheric gravity wave parameters based on satellite limb soundings. *Earth System Science Data*, **10**, 857–892. https://doi.org/10.5194/essd-10-857-2018

Ern, M., Preusse, P., Alexander, M. J., & Warner, C. D. (2004). Absolute values of gravity wave momentum flux derived from satellite data. *Journal Geophysical Research*, **109**, D20103. https://doi.org/10.1029/2004JD004752

Geller, M. A., Alexander, M. J., Love, P. T., Bacmeister, J., Ern, M., Hertzog, A., et al. (2013). A Comparison between Gravity Wave Momentum Fluxes in Observations and Climate Models. *Journal of Climate*, **26**(17), 6383–6405. https://doi.org/10.1175/jcli-d-12-00545.1

GFD Dennou Club. (2018). Dennou Club Library (version 7.3.4) [Software]. Retrieved from https://www.gfd-dennou.org/library/dcl/

Gille, J., Barnett, J., Whitney, J., Dials, M., Woodard, D., Rudolf, W., Lambert, A., & Mankin, W. (2003). The High Resolution Dynamics Limb Sounder (HIRDLS) Experiment on Aura. *Proceedings of SPIE*, **5152**, 162–171.

Gille, J. C., Barnett, J., Arter, P., Barker, M., Bernath, P., Boone, C., et al. (2008). High Resolution Dynamics Limb Sounder: Experiment overview, recovery, and validation of initial temperature data. *Journal of Geophysical Research*, **113**, D16S43. https://doi.org/10.1029/2007JD008824

Hersbach, H., Bell, B., Berrisford, P., Hirahara, S.., Horányi, A.., Muñoz-Sabater, J., et al. (2020). The ERA5 global reanalysis. *Quarterly Journal of the Royal Meteorological Society*. **146**, 1999–2049. https://doi.org/10.1002/qj.3803

Hindley, N. P., Wright, C. J., Gadian, A. M., Hoffmann, L., Hughes, J. K., Jackson, D. R., et al. (2021). Stratospheric gravity waves over the mountainous island of South Georgia: testing a high-resolution dynamical model with 3-D satellite observations and

radiosondes. *Atmospheric Chemistry and Physics*, **21**, 7695–7722. https://doi.org/10.5194/acp-21-7695-2021

Hindley, N. P., Wright, C. J., Hoffmann, L., Moffat-Griffin, T., & Mitchell, N. J. (2020). An 18-year climatology of directional stratospheric gravity wave momentum flux from 3-D satellite observations. *Geophysical Research Letters*, **47**, e2020GL089557. https://doi.org/10.1029/2020GL089557

Hindley, N. P., Wright, C. J., Smith, N. D., Hoffmann, L., Holt, L. A., Alexander, M. J., Moffat-Griffin, T., & Mitchell, N. J. (2019). Gravity waves in the winter stratosphere over the Southern Ocean: high-resolution satellite observations and 3-D spectral analysis. *Atmospheric Chemistry and Physics*, **19**, 15377–15414. https://doi.org/10.5194/acp-19-15377-2019

Hoffmann, L., & Alexander, M. J. (2009). Retrieval of stratospheric temperatures from Atmospheric Infrared Sounder radiance measurements for gravity wave studies. *Journal of Geophysical Research*, **114**, D07105. https://doi.org/10.1029/2008JD011241

Hoffmann, L., Alexander, M. J., Clerbaux, C., Grimsdell, A. W., Meyer, C. I., Rößler, T., & Tournier, B. (2014). Intercomparison of stratospheric gravity wave observations with AIRS and IASI. *Atmospheric Measurement Techniques*, **7**, 4517–4537. https://doi.org/10.5194/amt-7-4517-2014

Jones, W. L. (1969). Ray tracing for internal gravity waves. *Journal of Geophysical Research*, **74**, 2028–2033. https://doi.org/10.1029/JB074i008p02028

Kodera, K., Eguchi, N., Lee, J. N., Kuroda, Y., & Yukimoto, S. (2011). Sudden changes in the tropical stratospheric and tropospheric circulation during January 2009. *Journal of the Meteorological Society of Japan*, **89**(3), 283–290. https://doi.org/10.2151/jmsj.2011-308

Kodera, K., Mukougawa, H., & Kuroda, Y. (2011). A General Circulation Model Study of the Impact of a Stratospheric Sudden Warming Event on Tropical Convection. *SOLA*, **7**, 197–200. https://doi.org/10.2151/sola.2011-050

Körnich, H., & Becker, E. (2010). A simple model for the interhemispheric coupling of the middle atmosphere circulation. *Advances in Space Research*, **45**(5), 661–668.

Koshin, D., Sato, K., Kohma, M., & Watanabe, S. (2022). An update on the 4D-LETKF data assimilation system for the whole neutral atmosphere. *Geoscientific Model Development*, **15**, 2293–2307. https://doi.org/10.5194/gmd-15-2293-2022

Koshin, D., Sato, K., Miyazaki, K., & Watanabe, S. (2020). An ensemble Kalman filter data assimilation system for the whole neutral atmosphere. *Geoscientific Model Development*, **13**, 3145–3177. https://doi.org/10.5194/gmd-13-3145-2020

Kruse, C. G., Alexander, M. J., Hoffmann, L., van Niekerk, A., Polichtchouk, I., Bacmeister, J. T., et al. (2022). Observed and Modeled Mountain Waves from the Surface to the Mesosphere near the Drake Passage. *Journal of the Atmospheric Sciences*, **79**(4), 909–932. https://doi.org/10.1175/JAS-D-21-0252.1

Limpasuvan, V., Y. J. Orsolini, A. Chandran, R. R. Garcia, & A. K. Smith (2016). On the composite response of the MLT to major sudden stratospheric warming events with elevated stratopause. *Journal of Geophysical Research: Atmospheres*, **121**, 4518–4537. https://doi.org/10.1002/2015JD024401

Limpasuvan, V., Richter, J. H., Orsolini, Y. J., Stordal, F., & Kvissel, O.-K. (2012). The roles of planetary and gravity waves during a major stratospheric sudden warming as characterized by WACCM. *Journal of Atmospheric and Solar-Terrestrial Physics*, **78**–**79**, 84–98. https://doi.org/10.1016/j.jastp.2011.03.004

Manney, G. L., Krüger, K., Pawson, S., Minschwaner, K., Schwartz, M. J., Daffer, W. H., et al. (2008). The evolution of the stratopause during the 2006 major warming: Satellite data and assimilated meteorological analyses. *Journal of Geophysical Research*, **113**(D11), D11115. https://doi.org/10.1029/2007JD009097

Manney, G. L., Schwartz, M. J., Krüger, K., Santee, M. L., Pawson, S., Lee, J. N., Daffer, W. H., Fuller, R. A., & Livesey, N. J. (2009). Aura Microwave Limb Sounder observations of dynamics and transport during the record-breaking 2009 Arctic stratospheric major warming. *Geophysical Research Letters*, **36**, L12815. https://doi.org/10.1029/2009GL038586

MathWorks (2022). MATLAB (Version R2022b). [Software]. Retrieved from https://jp.mathworks.com/products/matlab.html

Meyer, C. I., Ern, M., Hoffmann, L., Trinh, Q. T., & Alexander, M. J. (2018). Intercomparison of AIRS and HIRDLS stratospheric gravity wave observations. *Atmospheric Measurement Techniques*, **11**(1), 215–232. https://doi.org/10.5194/amt-11-215-2018

Okui, H., Sato, K., Koshin, D., & Watanabe, S. (2021). Formation of a mesospheric inversion layer and the subsequent elevated stratopause associated with the major stratospheric sudden warming in 2018/19. *Journal of Geophysical Research: Atmospheres*, **126**, e2021JD034681. https://doi.org/10.1029/2021JD034681

Okui, H., Sato, K., & Watanabe, S. (2022). Contribution of gravity waves to universal vertical wavenumber (~m−3) spectra revealed by a gravity-wave-permitting general circulation model. *Journal of Geophysical Research: Atmospheres*, **127**(10), e2021JD036222. https://doi.org/10.1029/2021JD036222

Plougonven, R., & Zhang, F. (2014). Internal gravity waves from atmospheric jets and fronts. *Reviews of Geophysics*, **52**, 33–76. https://doi.org/10.1002/2012RG000419

Randel, W. J. (1993). Global Variations of Zonal Mean Ozone during Stratospheric Warming Events. *Journal of Atmospheric Sciences*, **50**(19), 3308–3321. https://doi.org/10.1175/1520-0469(1993)050%3C3308:GVOZMO%3E2.0.CO;2

Rao, J., Garfinkel, C. I., Chen, H., & White, I. P. (2019). The 2019 New Year stratospheric sudden warming and its real-time predictions in multiple S2S models. *Journal of Geophysical Research: Atmospheres*, **124**, 11155–11174. https://doi.org/10.1029/2019JD030826

Sato, K., & Dunkerton, T. J. (1997). Estimates of momentum flux associated with equatorial Kelvin and gravity waves. *Journal of Geophysical Research*, **102**, 26247–26261. https://doi.org/10.1029/96JD02514

Sato, K., Tateno, S., Watanabe, S., & Kawatani, Y. (2012). Gravity Wave characteristics in the Southern Hemisphere revealed by a high-resolution middle-atmosphere general circulation model. *Journal of the Atmospheric Sciences*, **69**(4), 1378–1396. https://doi.org/10.1175/jas-d-11-0101.1

Sato, K., Watanabe, S., Kawatani, Y., Tomikawa, Y., Miyazaki, K., & Takahashi, M. (2009). On the origins of mesospheric gravity waves. *Geophysical Research Letters*, **36**, L19801. https://doi.org/10.1029/2009GL039908

Siskind, D. E., Eckermann, S. D., McCormack, J. P., Coy, L., Hoppel, K. W., & Baker, N. L. (2010). Case studies of the mesospheric response to recent minor, major, and extended stratospheric warmings. *Journal of Geophysical Research*, **115**, D00N03. https://doi.org/10.1029/2010JD014114

Smith, A. K., Pedatella, N. M., & Mullen, Z. K. (2020). Interhemispheric Coupling Mechanisms in the Middle Atmosphere of WACCM6. *Journal of the Atmospheric Sciences*, **77**(3), 1101–1118. https://doi.org/10.1175/JAS-D-19-0253.1

Stockwell, R. G., Mansinha, L., & Lowe, R. P. (1996). Localization of the complex spectrum: The S transform. *IEEE Transactions on Signal Processing*, **44**(4), 998–1001. https://doi.org/10.1109/78.492555

Thurairajah, B., Bailey, S. M., Cullens, C. Y., Hervig, M. E., & Russell, J. M. (2014). Gravity wave activity during recent stratospheric sudden warming events from SOFIE temperature measurements. *Journal of Geophysical Research: Atmospheres*, **119**, 8091–8103, doi:10.1002/2014JD021763.

Tomikawa, Y., Sato, K., Watanabe, S., Kawatani, Y., Miyazaki, K., & Takahashi, M. (2012). Growth of planetary waves and the formation of an elevated stratopause after a major stratospheric sudden warming in a T213L256 GCM. *Journal of Geophysical Research*, **117**, D16101. https://doi.org/10.1029/2011JD017243

Vadas, S. L., & Becker, E. (2018). Numerical modeling of the excitation, propagation, and dissipation of primary and secondary gravity waves during wintertime at McMurdo Station in the Antarctic. *Journal of Geophysical Research: Atmospheres*, **123**, 9326–9369. https://doi.org/10.1029/2017JD027974

Watanabe, S., Kawatani, Y., Tomikawa, Y., Miyazaki, K., Takahashi, M., & Sato, K. (2008). General aspects of a T213L256 middle atmosphere general circulation model. *Journal of Geophysical Research: Atmospheres*, **113**(D12). https://doi.org/10.1029/2008jd010026

Watanabe, S., Koshin, D., Noguchi, S., & Sato, K. (2022). Gravity wave morphology during the 2018 sudden stratospheric warming simulated by a whole neutral atmosphere general circulation model. *Journal of Geophysical Research: Atmospheres*, **127**, e2022JD036718. https://doi.org/10.1029/2022JD036718

Watanabe, S., & Miyahara, S. (2009). Quantification of the gravity wave forcing of the migrating diurnal tide in a gravity wave-resolving general circulation model. *Journal of Geophysical Research: Atmospheres*, **114**, D07110. https://doi.org/10.1029/2008JD011218

Wright, C. (2010). Detection of stratospheric gravity waves using HIRDLS data [PhD thesis]. University of Oxford.

Wright, C. J., Hindley, N. P., Alexander, M. J., Holt, L. A., & Hoffmann, L. (2021). Using vertical phase differences to better resolve 3D gravity wave structure. *Atmospheric Measurement Techniques*, **14**, 5873–5886, https://doi.org/10.5194/amt-14-5873-2021

Wright, C. J., Hindley, N. P., Hoffmann, L., Alexander, M. J., & Mitchell, N. J. (2017). Exploring gravity wave characteristics in 3-D using a novel S-transform technique: AIRS/Aqua measurements over the Southern Andes and Drake Passage. *Atmospheric Chemistry and Physics*, **17**, 8553–8575. https://doi.org/10.5194/acp-17-8553-2017

Wright, C. J., Hindley, N. P., & Mitchell, N. J. (2016a). Combining AIRS and MLS observations for three-dimensional gravity wave measurement. *Geophysical Research Letters*, **43**, 884–893, https://doi.org/10.1002/2015GL067233

Wright, C. J., Hindley, N. P., Moss, A. C., & Mitchell, N. J. (2016b). Multi-instrument gravity-wave measurements over Tierra del Fuego and the Drake Passage – Part 1: Potential energies and vertical wavelengths from AIRS, COSMIC, HIRDLS, MLS-Aura,

SAAMER, SABER and radiosondes. *Atmospheric Measurement Techniques*, **9**, 877–908. https://doi.org/10.5194/amt-9-877-2016

Wright, C. J., Osprey, S. M., Barnett, J. J., Gray, L. J., & Gille, J. C. (2010). High Resolution Dynamics Limb Sounder measurements of gravity wave activity in the 2006 Arctic stratosphere. *Journal of Geophysical Research*, **115**, D02105. https://doi.org/10.1029/2009JD011858

Wright, C. J., Rivas, M. B., & Gille, J. C. (2011). Intercomparisons of HIRDLS, COSMIC and SABER for the detection of stratospheric gravity waves. *Atmospheric Measurement Techniques*, **4**, 1581–1591, https://doi.org/10.5194/amt-4-1581-2011

Yasuda, Y., Sato, K., & Sugimoto, N. (2015). A Theoretical Study on the Spontaneous Radiation of Inertia–Gravity Waves Using the Renormalization Group Method. Part I: Derivation of the Renormalization Group Equations. *Journal of the Atmospheric Sciences*, **72**(3), 957-983. https://doi.org/10.1175/JAS-D-13-0370.1

Yasui, R., Sato, K., & Miyoshi, Y. (2021). Roles of Rossby Waves, Rossby–Gravity Waves, and Gravity Waves Generated in the Middle Atmosphere for Interhemispheric Coupling. *Journal of the Atmospheric Sciences*, **78**(12), 3867–3888. https://doi.org/10.1175/JAS-D-21-0045.1

Yoshida, K., & Mizuta, R. (2021). Do sudden stratospheric warmings boost convective activity in the tropics? *Geophysical Research Letters*, **48**, e2021GL093688. https://doi.org/10.1029/2021GL093688

Zhang, J., Tian, W., Chipperfield, M., Xie, F., & Huang, J. (2016). Persistent shift of the Arctic polar vortex towards the Eurasian continent in recent decades. *Nature Climate Change*, **6**, 1094–1099. https://doi.org/10.1038/nclimate3136

782 **Figure 1**. Zonal wind at a geopotential height of z= 39 km during (a) 15–22 December 2018
783 (Period 1), (b) 23–31 December 2018 (Period 2), and (c) 1–8 January 2019 (Period 3) obtained
784 from JAGUAR. An Arctic major SSW occurred on 1 January 2019, the first day of Period 3.
785

786 **Figure 2**. (a, b) Amplitudes and (c, d) zonal and (e, f) meridional momentum flux of dominant
787 GWs at z= 39 km averaged over 15–22 December 2018 (Period 1). Panels (a, c, e) and (b, d, f)
788 show the results from the AIRS observations and the JAGUAR data, respectively. The right
789 elongated panels display the zonal mean of the values shown in the respective panels on the left
790 side.
791

792 **Figure 3**. As in Fig. 2 but for 23–31 December 2018 (Period 2).
793

794 **Figure 4**. As in Fig. 2 but for 1–8 January 2019 (Period 3).
795

796 **Figure 5**. (a) Amplitudes, (b) vertical wavelengths λ_z, and (c) zonal and (d) meridional
797 momentum flux of dominant GWs at z= 39 km estimated from the JAGUAR data without the
798 AIRS observational filter applied. The right elongated panels display the zonal mean of the
799 values shown in the left respective ones. Note that the color scales for the maps and the
800 horizontal axes for the curves are different from those in Figs. 2–4. Two circles in panels (a) and
801 (b) denote the regions where the GW amplitudes are especially large relative to those in the
802 JAGUAR data with the observational filter (Fig. 2b). A dashed curve in panel (b) represents the
803 path of the eastward jet, as shown in Fig. 1a.
804

805 **Figure 6**. North Pole map of the absolute horizontal wind speed averaged over Period 1 obtained
806 from JAGUAR data. The polar vortex is displaced toward the Eurasian Continent with two jet
807 streaks from Europe to the Central Asia and from the East Asia to Greenland.
808

809 **Figure 7**. Temperature perturbations at z= 39 km in AIRS granules (a–c) in Europe at 1:54 UTC
810 on 22 December (Case 1), (d–f) in eastern Eurasia at 20:36 UTC on 16 December (Case 2), and
811 (g–i) to the east of Madagascar at 21:12 UTC on 20 December (Case 3). Panels (a, d, g), (b, e, h),
812 and (c, f, i) show the results from the AIRS observations, JAGUAR with the observational filter,
813 and JAGUAR without the observational filter, respectively. Panel (j) provides the location of the
814 regions shown in panels (a–i) on Fig. 2a.
815

816 **Figure 8**. Results from the 3-D S-transform for Case 2. Panels (a–d) show the horizontal maps at
817 z= 39 km and panels (e–h) show the latitude-altitude sections at 105° E of (a, e) amplitudes, (b,
818 f) λ_z, and (c, g) zonal and (d, h) meridional momentum flux. Vertical (horizontal) lines in the top
819 (bottom) panels denote the longitude (altitude) of the bottom (top) panels.
820

821 **Figure 9**. Latitude-altitude section at 105° E of (a) zonal wind and (b) the buoyancy frequency
822 $N = \sqrt{(\mathrm{g}/\overline{T})(d\overline{T}/dz)}$ for Case 2 obtained from the JAGUAR data.
823

Figure 1.

U at z=39km

(a) 15–22 DEC 2018

90N
60N
30N
EQ
30S
60S
90S
180 120W 60W 0 60E 120E 180

(b) 23–31 DEC 2018

90N
60N
30N
EQ
30S
60S
90S
180 120W 60W 0 60E 120E 180

(c) 1–8 JAN 2019

90N
60N
30N
EQ
30S
60S
90S
180 120W 60W 0 60E 120E 180

(m/s)
100
80
60
40
20
0
−20
−40
−60
−80
−100

Figure 2.

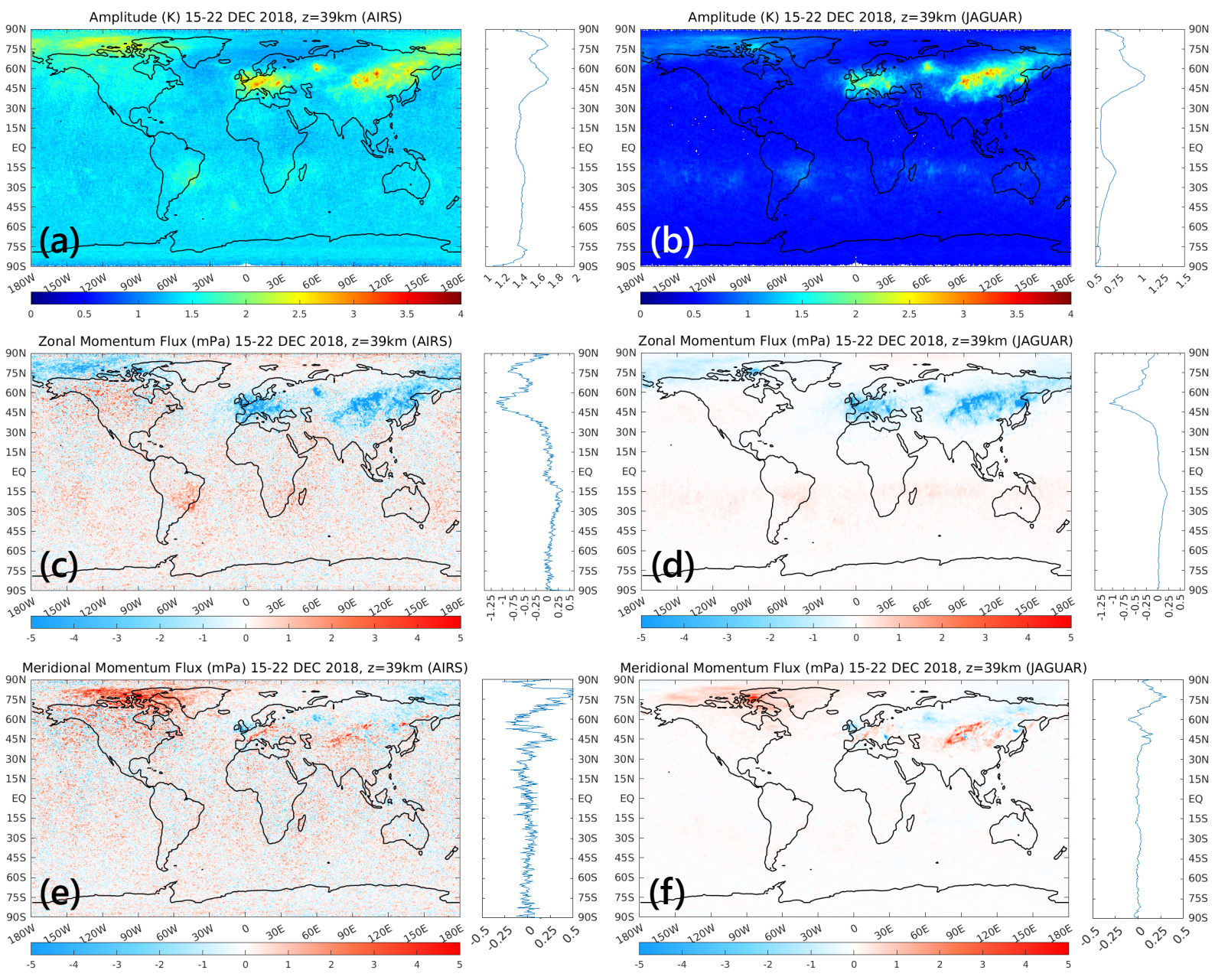
Amplitude (K) 15-22 DEC 2018, z=39km (AIRS)
Amplitude (K) 15-22 DEC 2018, z=39km (JAGUAR)
Zonal Momentum Flux (mPa) 15-22 DEC 2018, z=39km (AIRS)
Zonal Momentum Flux (mPa) 15-22 DEC 2018, z=39km (JAGUAR)
Meridional Momentum Flux (mPa) 15-22 DEC 2018, z=39km (AIRS)
Meridional Momentum Flux (mPa) 15-22 DEC 2018, z=39km (JAGUAR)
(a)
(b)
(c)
(d)
(e)
(f)

Figure 3.

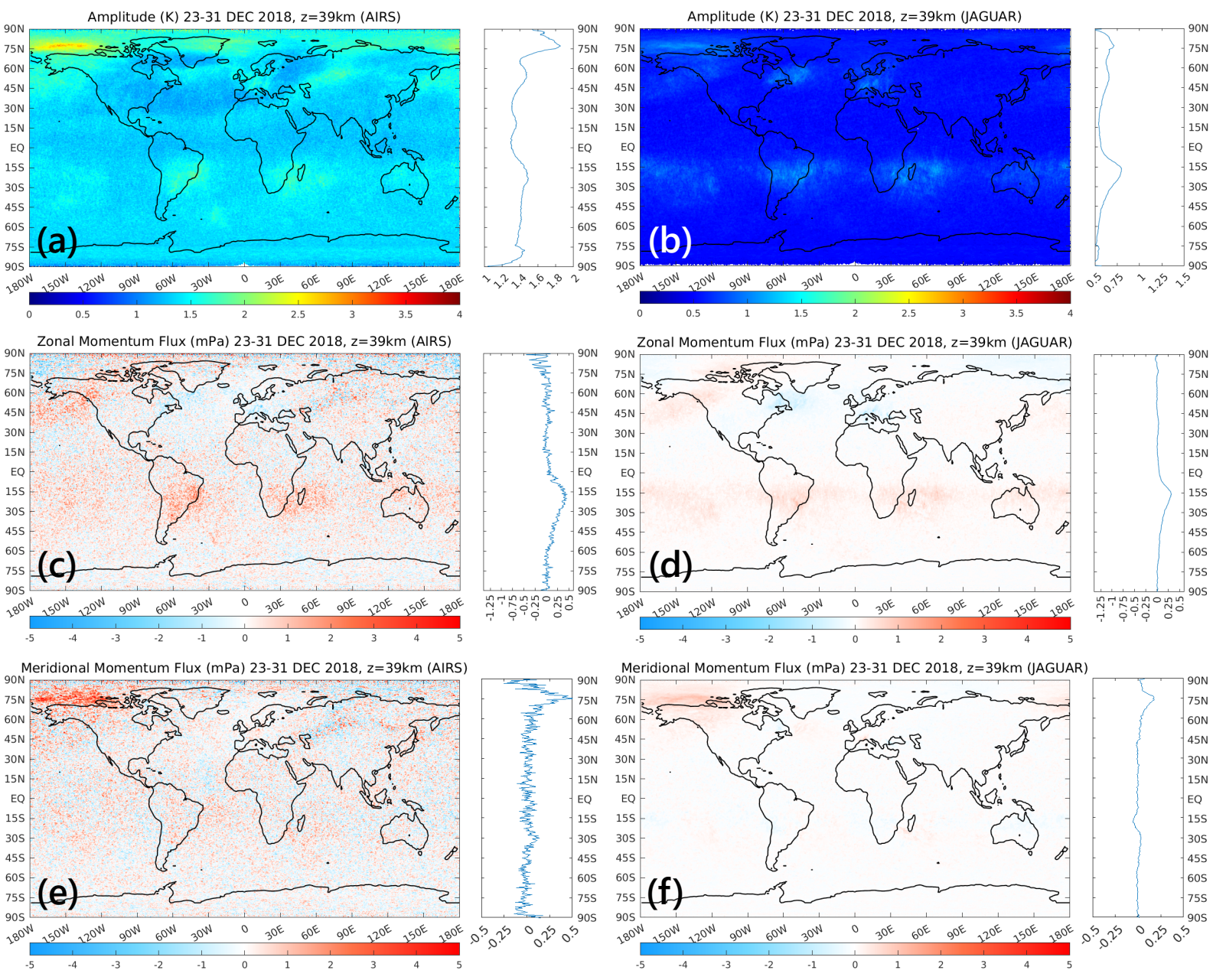
Amplitude (K) 23-31 DEC 2018, z=39km (AIRS)
Amplitude (K) 23-31 DEC 2018, z=39km (JAGUAR)
Zonal Momentum Flux (mPa) 23-31 DEC 2018, z=39km (AIRS)
Zonal Momentum Flux (mPa) 23-31 DEC 2018, z=39km (JAGUAR)
Meridional Momentum Flux (mPa) 23-31 DEC 2018, z=39km (AIRS)
Meridional Momentum Flux (mPa) 23-31 DEC 2018, z=39km (JAGUAR)
(a)
(b)
(c)
(d)
(e)
(f)
90N 75N 60N 45N 30N 15N EQ 15S 30S 45S 60S 75S 90S
180W 150W 120W 90W 60W 30W 0 30E 60E 90E 120E 150E 180E

Figure 4.

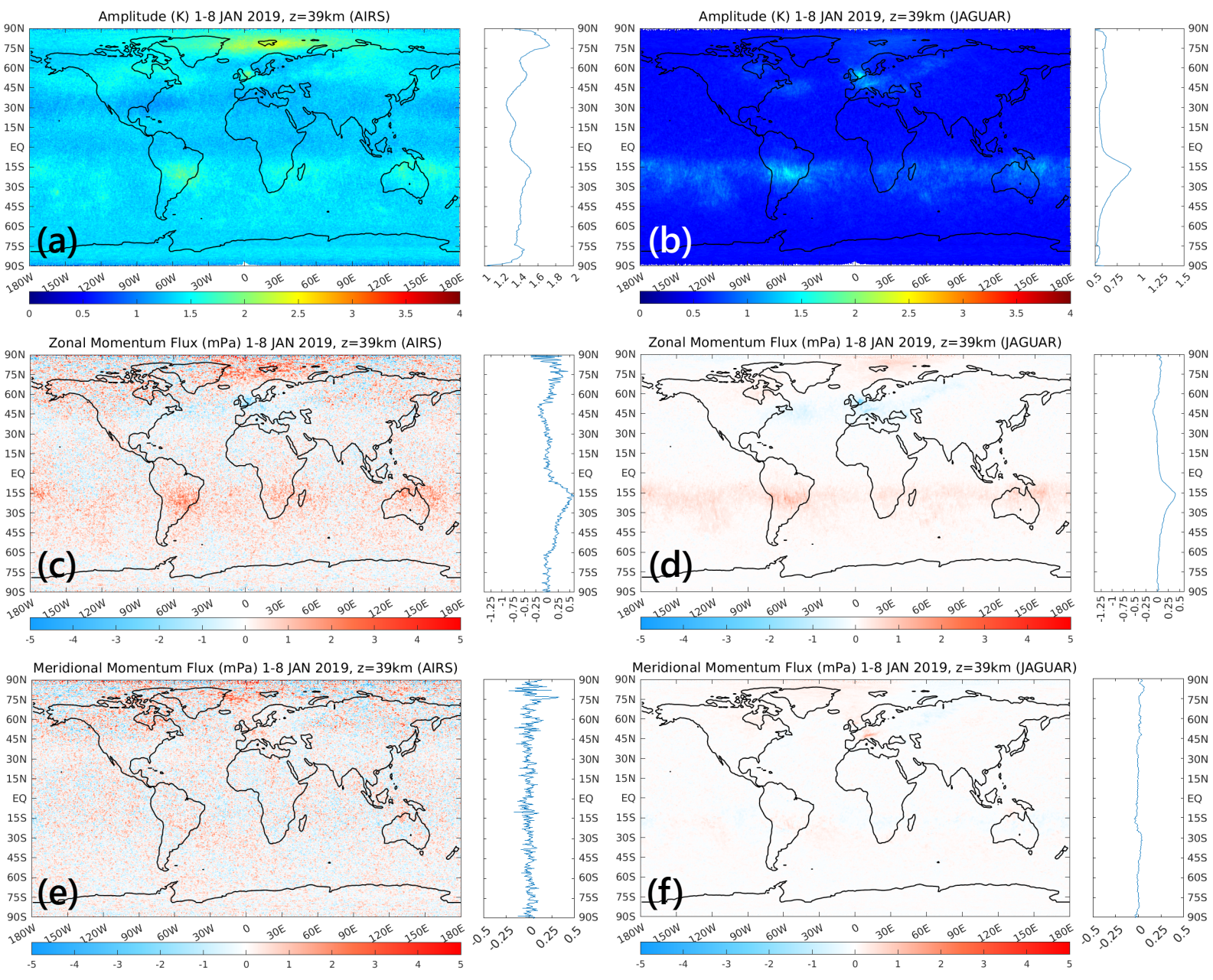
Amplitude (K) 1-8 JAN 2019, z=39km (AIRS)
Amplitude (K) 1-8 JAN 2019, z=39km (JAGUAR)
Zonal Momentum Flux (mPa) 1-8 JAN 2019, z=39km (AIRS)
Zonal Momentum Flux (mPa) 1-8 JAN 2019, z=39km (JAGUAR)
Meridional Momentum Flux (mPa) 1-8 JAN 2019, z=39km (AIRS)
Meridional Momentum Flux (mPa) 1-8 JAN 2019, z=39km (JAGUAR)
(a)
(b)
(c)
(d)
(e)
(f)
90N 75N 60N 45N 30N 15N EQ 15S 30S 45S 60S 75S 90S
180W 150W 120W 90W 60W 30W 0 30E 60E 90E 120E 150E 180E

Figure 5.

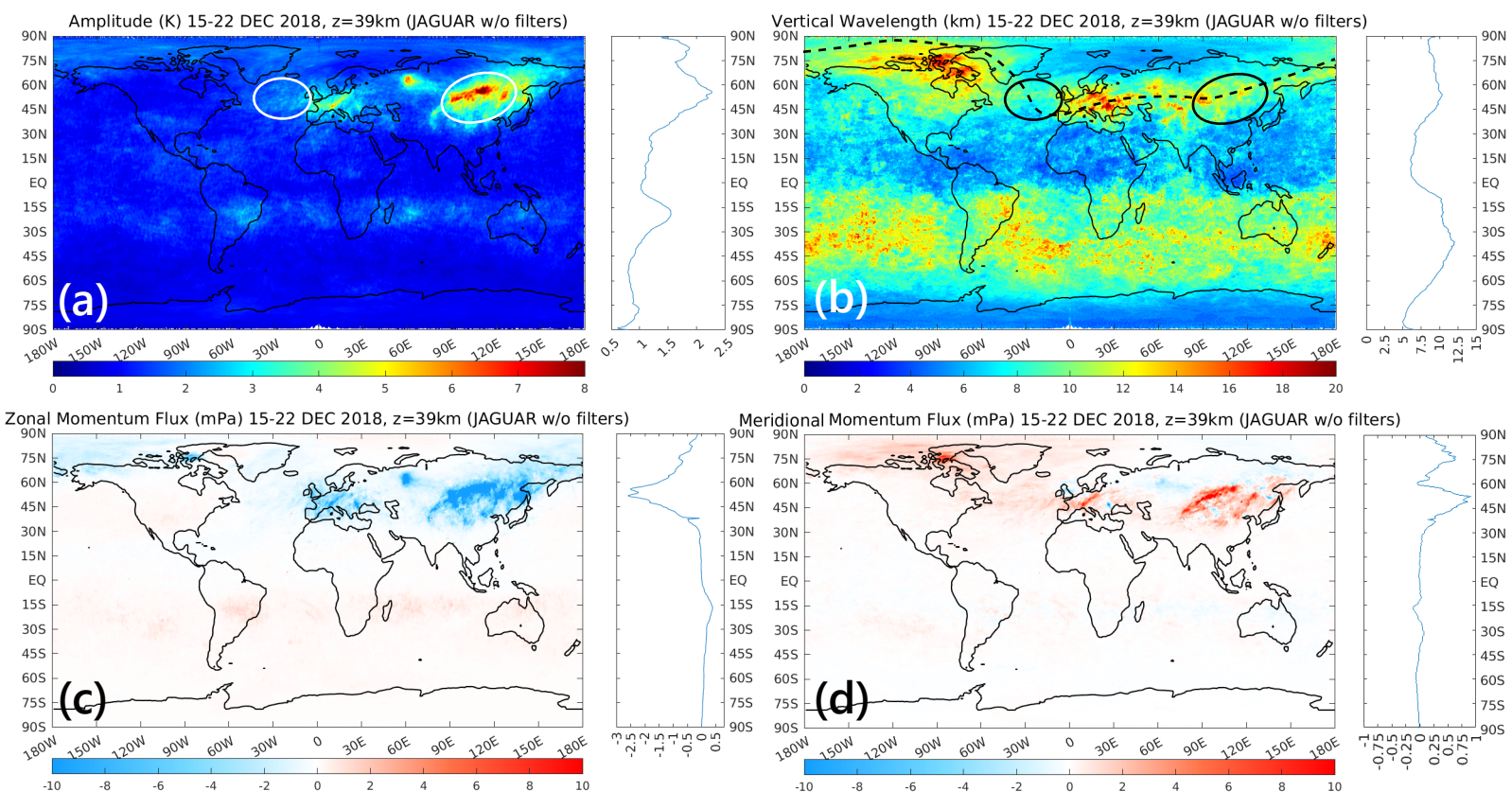
Amplitude (K) 15-22 DEC 2018, z=39km (JAGUAR w/o filters)
Vertical Wavelength (km) 15-22 DEC 2018, z=39km (JAGUAR w/o filters)
Zonal Momentum Flux (mPa) 15-22 DEC 2018, z=39km (JAGUAR w/o filters)
Meridional Momentum Flux (mPa) 15-22 DEC 2018, z=39km (JAGUAR w/o filters)
(a)
(b)
(c)
(d)
90N 75N 60N 45N 30N 15N EQ 15S 30S 45S 60S 75S 90S
180W 150W 120W 90W 60W 30W 0 30E 60E 90E 120E 150E 180E
0 1 2 3 4 5 6 7 8
0.5 1 1.5 2 2.5
0 2 4 6 8 10 12 14 16 18 20
0 2.5 5 7.5 10 12.5 15
-10 -8 -6 -4 -2 0 2 4 6 8 10
-3 -2.5 -2 -1.5 -1 -0.5 0 0.5
-10 -8 -6 -4 -2 0 2 4 6 8 10
-1 -0.75 -0.5 -0.25 0 0.25 0.5 0.75 1

Figure 6.

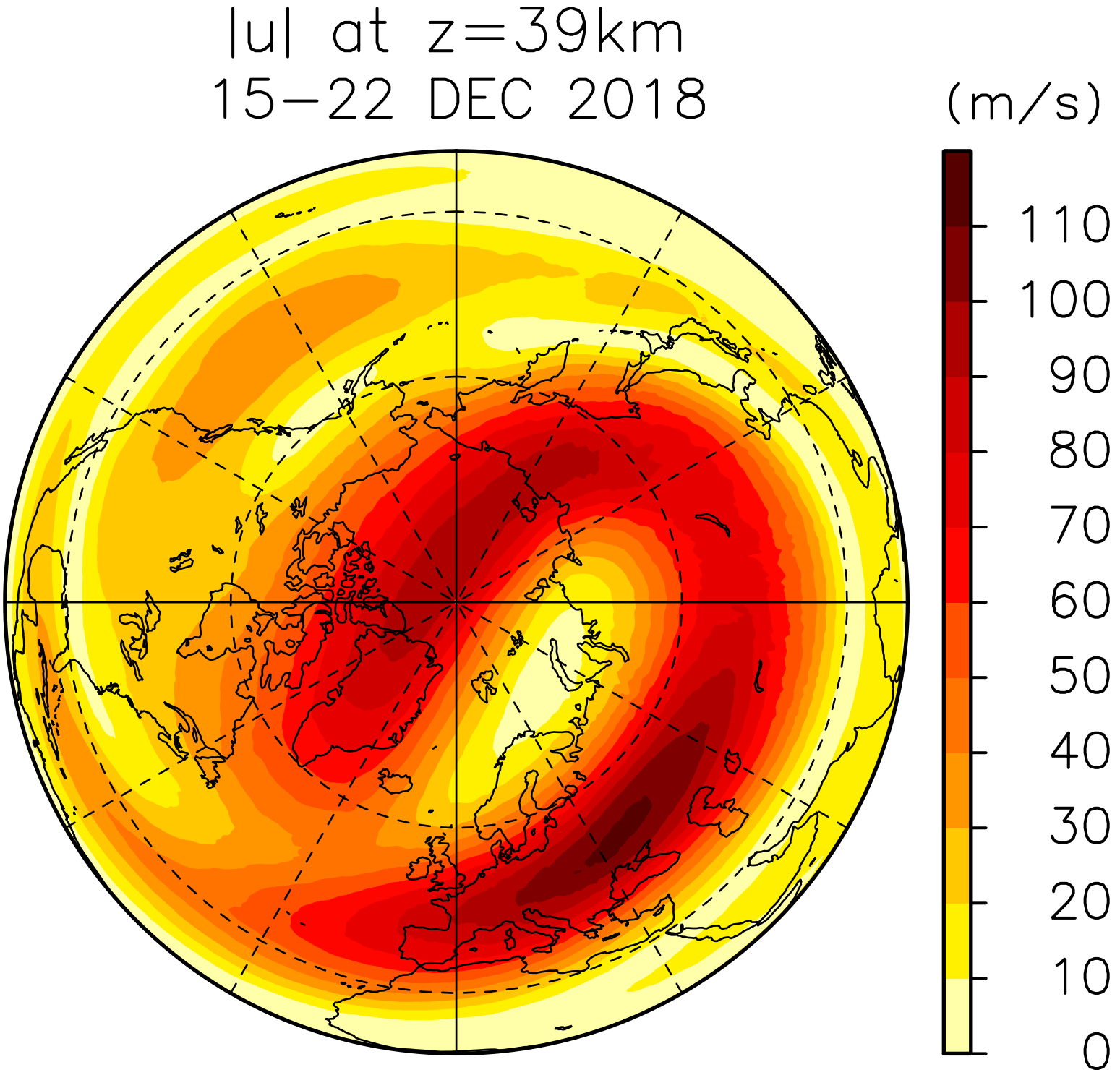
|u| at z=39km
15–22 DEC 2018
(m/s)
110
100
90
80
70
60
50
40
30
20
10
0

Figure 7.

AIRS

(a) 01:54UTC 22 DEC 2018

JAGUAR w/ obs. filter

(b) 01:30UTC 22 DEC 2018

JAGUAR w/o obs. filter

(c) 01:30UTC 22 DEC 2018

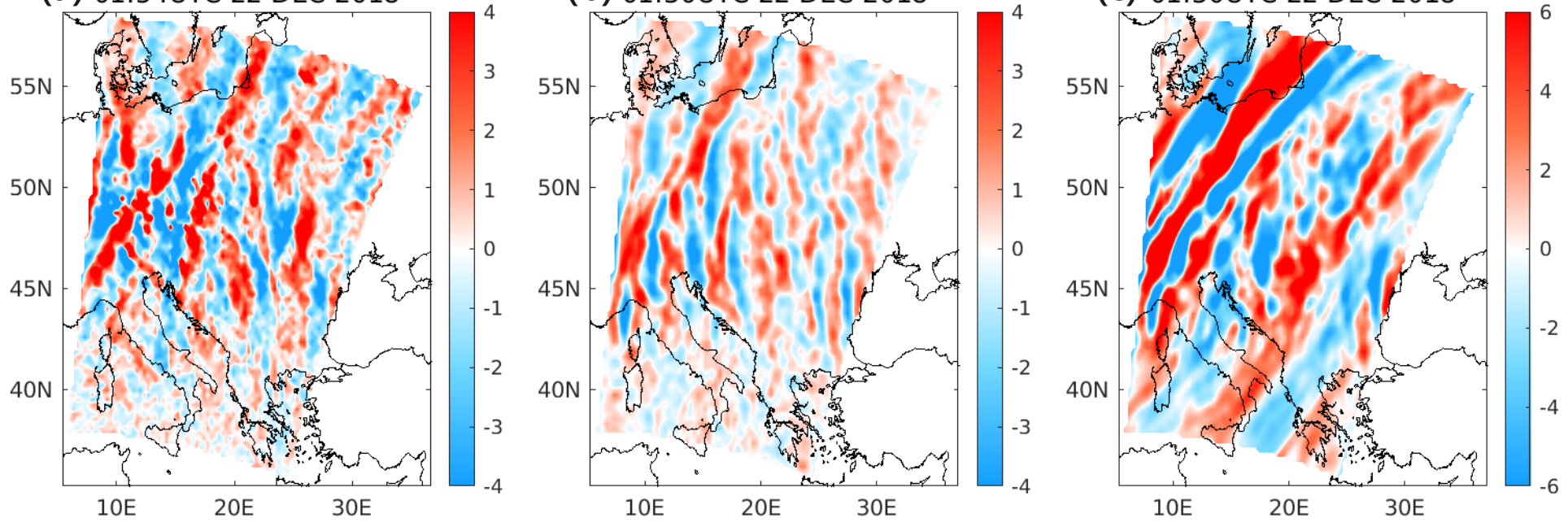

(d) 20:36UTC 16 DEC 2018

(e) 20:30UTC 16 DEC 2018

(f) 20:30UTC 16 DEC 2018

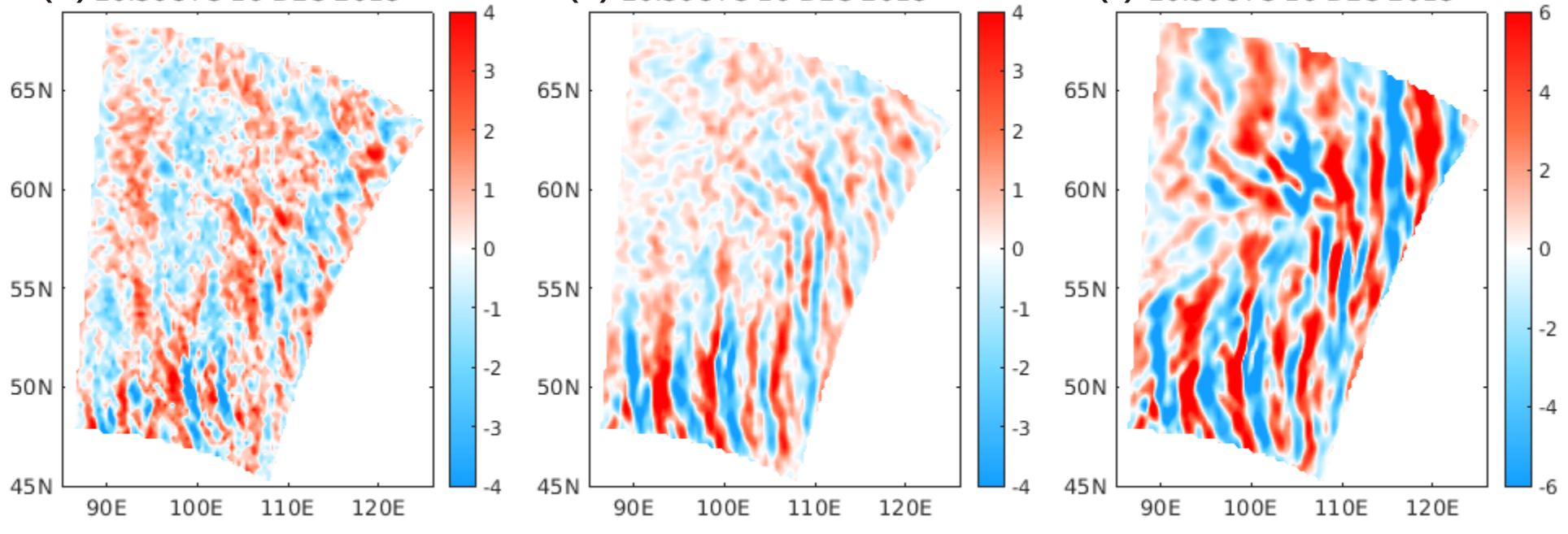

(g) 21:12UTC 20 DEC 2018

(h) 21:30UTC 20 DEC 2018

(i) 21:30UTC 20 DEC 2018

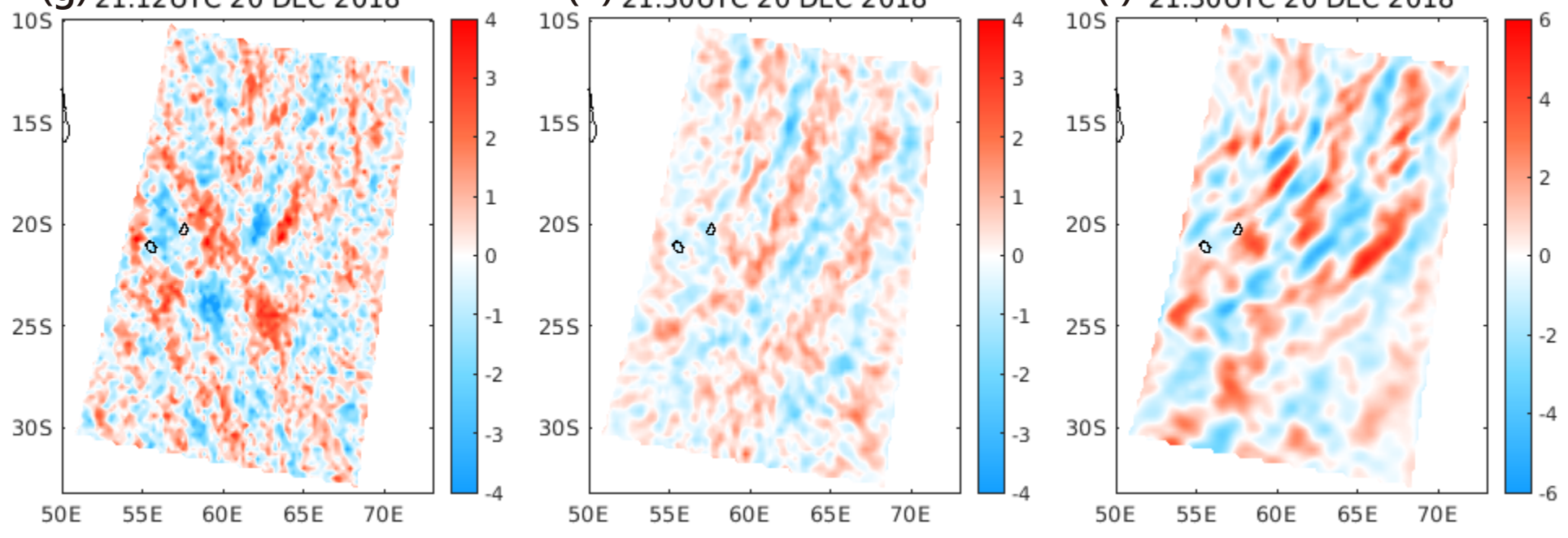

(j) Amplitude (K) 15-22 DEC 2018, z=39km (AIRS)

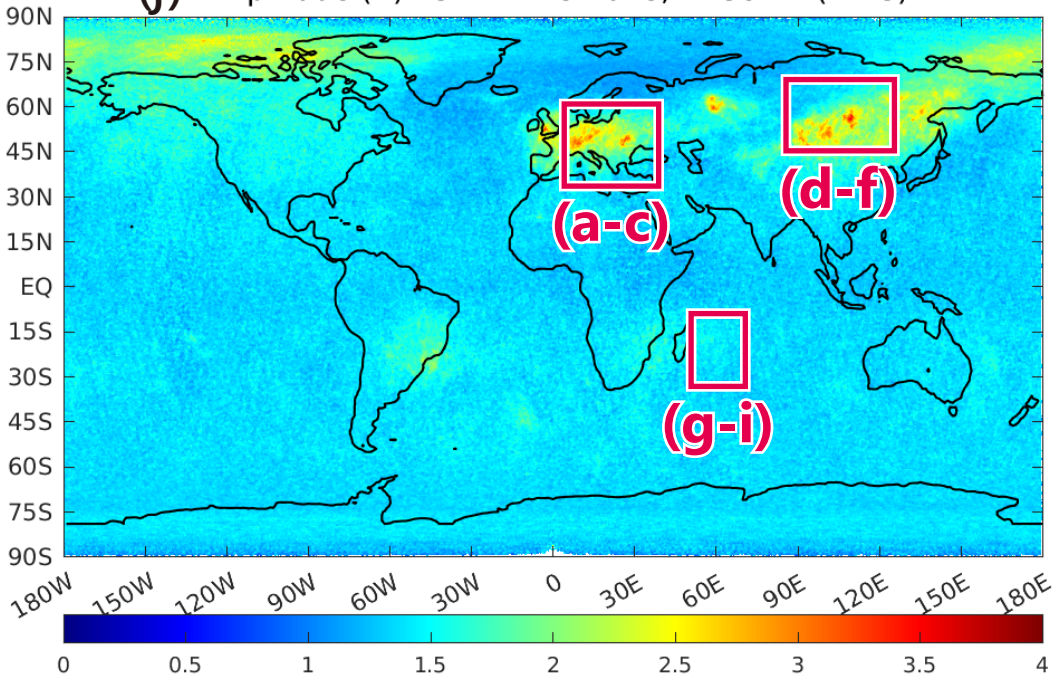

Figure 8.

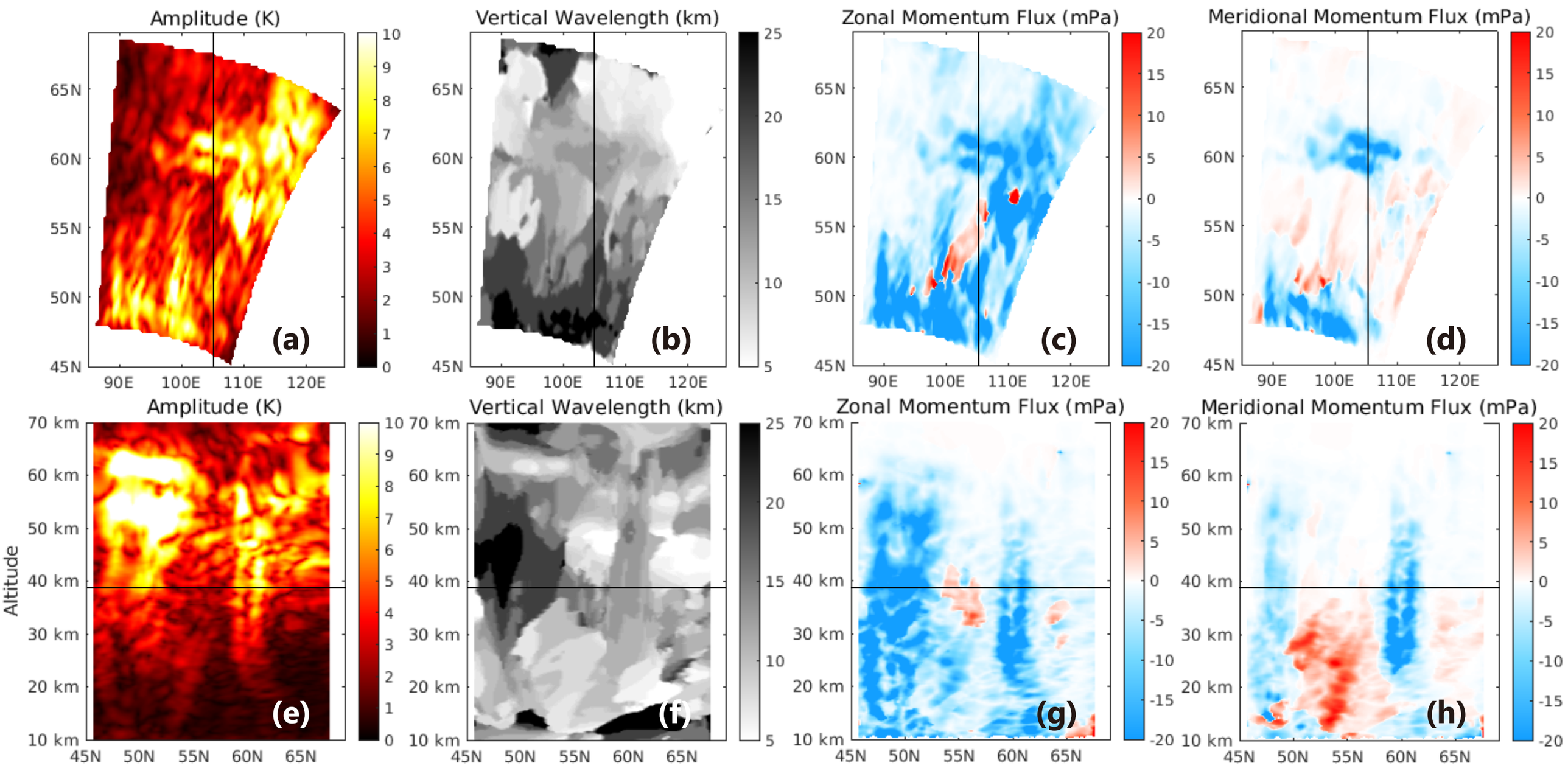
Amplitude (K)
Vertical Wavelength (km)
Zonal Momentum Flux (mPa)
Meridional Momentum Flux (mPa)
(a)
(b)
(c)
(d)
(e)
(f)
(g)
(h)
65N
60N
55N
50N
45N
90E
100E
110E
120E
70 km
60 km
50 km
40 km
30 km
20 km
10 km
Altitude
45N
50N
55N
60N
65N

Figure 9.

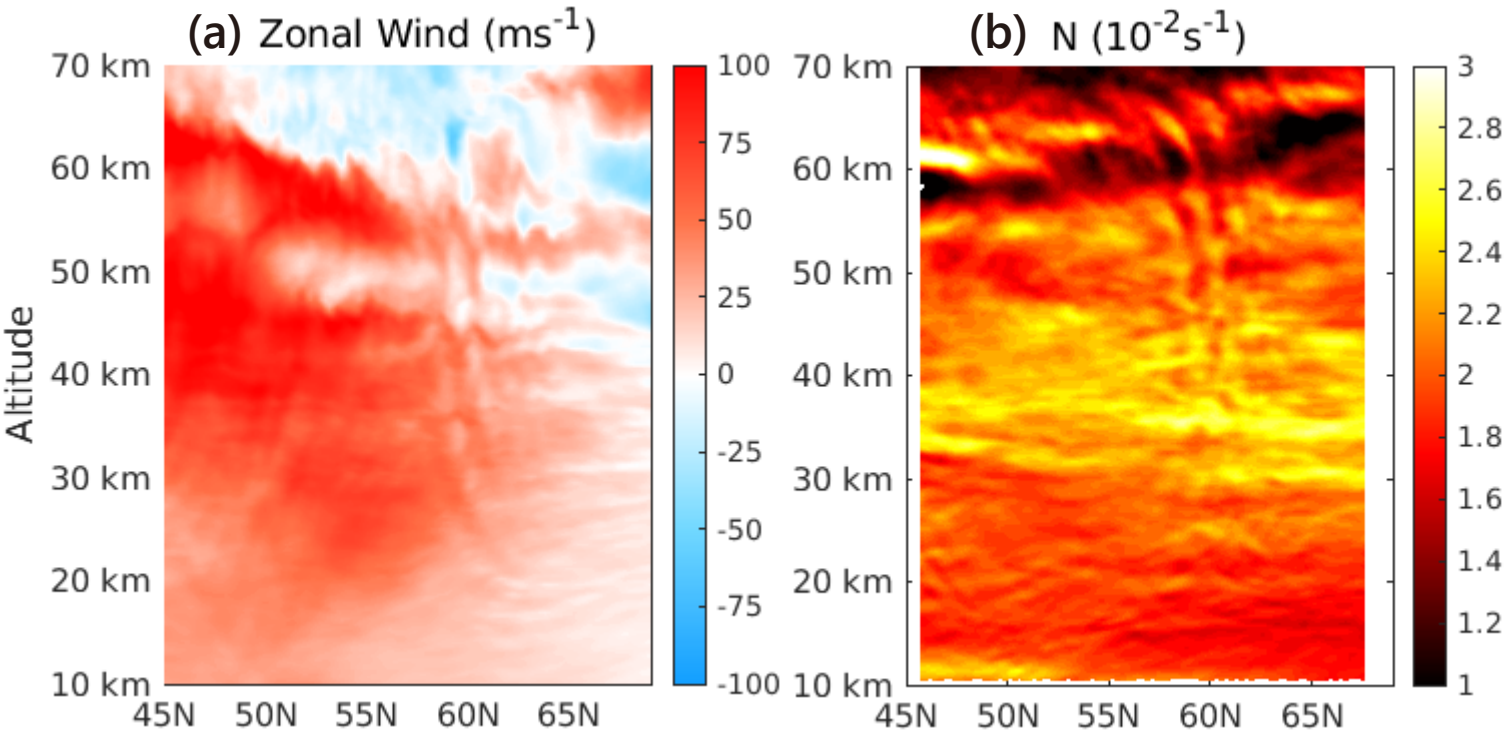
(a) Zonal Wind (ms^{-1})
(b) N (10^{-2}s^{-1})
Altitude
70 km
60 km
50 km
40 km
30 km
20 km
10 km
45N
50N
55N
60N
65N
100
75
50
25
0
-25
-50
-75
-100
3
2.8
2.6
2.4
2.2
2
1.8
1.6
1.4
1.2
1